Deriving slope movements for an imminent landslide along the Jinsha river

Wentao Yang[1], Lianyou Liu[2,3,4], Peijun Shi[2,3,4]

[1]Three-gorges Reservoir Area (Chongqing) Forest Ecosystem Research Station, School of Soil and Water Conservation, Beijing Forestry University, Beijing, 100083, China
[2]Academy of Disaster Reduction and Emergency Management, Ministry of Emergency Management & Ministry of Education, Beijing Normal University, Beijing, 100875, China
[3]MOE, Key Laboratory of Environmental Change and Natural Disaster, Beijing Normal University, Beijing, 100875, China
[4]State Key Laboratory of Earth Surface Processes and Resource Ecology, Beijing Normal University, Beijing, 100875, China

Correspondence to: Lianyou Liu (lyliu@bnu.edu.cn) and Peijun Shi (spj@bnu.edu.cn)

Abstract. Landslides are major hazards that may pose serious threats to mountain communities. Even landslides in remote mountains could have non-negligible impacts on populous regions by blocking large rivers and forming megafloods. Usually, there are slope deformations before major landslides occur, and detecting precursors over large mountain regions is important for screening possible landslide disasters. In this work, we applied multi-temporal optical remote sensing images (Landsat 7 and Sentinel-2) and an image correlation method to detect sub-pixel slope deformations of a slope. Along the Jinsha river, this slope is located downstream the famous Baige landslide near the Mindu town, Tibet Autonomous Region. We used DEM derived aspect to restrain background noises in image correlation results. We found the slope remained stable from November 2015 to November 2018 and moved significantly from November 2018 to November 2019. We used more data to analyse slope movement in 2019 and found retrogressive slope movements with increasingly large deformations near the river bank. We also analysed spatial-temporal patterns of the slope deformation from October 2018 to February 2020 and found seasonal variations in slope deformations. Only the slope foot moved in dry seasons, whereas the entire slope activated in rainy seasons. Until 24 August 2019, the size of the slope with displacements larger than 3 m is similar to that of the Baige landslide. However, the river width at the foot of this slope is much narrower than the river width at the foot of the Baige landslide. We speculate it may continue to slide down and could threaten the Jinsha river. Further modelling works should be done to check if the imminent landslide could dam the Jinsha river and measures be taken to mitigate possible dammed breach flood disasters. This work illustrates the potential of using optical remote sensing to monitor slope deformations over large remote mountain regions.

1 Introduction

Landslides are major natural hazards in mountain regions and causing widespread disasters every year around the globe (Petley 2012; Zhang et al. 2020). Precursors often occur before major landslides (Intrieri et al. 2018). Continuous monitoring of mountain slopes before major landslides occur is crucial for landslide disaster prevention (Luo et al. 2019).

On 10 October 2018, the major Baige landslide along the Jinsha River (upstream of the Yangtze River) occurred. This famous landslide blocked the river twice and caused two megafloods to downstream areas (Fan et al. 2019). Although the Baige landslide is located in a remote mountain region bordering the Tibet Autonomous Region and the Sichuan Province, the influence of the floods due to this landslide caused damages of infrastructures hundreds of kilometres downstream in Yunnan Province. To cope with possible disasters from the breaches of the landslide dammed lake, the government of Yunnan province initiated a level III response. Downstream disasters caused by the Baige landslide suggests that similar landslides on upstream rivers could cause damages to far downstream areas and possibly large scale slope movement before collapse should be closely monitored.

To monitor slope movement over large mountain regions, remote sensing techniques have been an efficient way (Du et al. 2020). Optical passive and microwave active radar remote sensing are the two most frequently used methods to detect slope displacements. Using InSAR techniques, active radar remote sensing can detect subtle slope movement from millimetres to a few decimetres (Intrieri et al. 2018; Samsonov et al. 2020). However, larger slope movement up to a few metres could lead to image incoherence in InSAR techniques (Wasowski and Bovenga 2014). In contrary, optical passive remote sensing is good at detecting larger slope movements that are visible on images (Bradley et al. 2019; Lacroix et al. 2020). In recent years, image correlation methods have been proposed and widely used to detect sub-pixel slope displacements in optical images (Bontemps et al. 2018; Lacroix et al. 2019; Lacroix et al. 2018; Yang et al. 2020).

In this work, using sub-pixel optical image correlation methods we report a landslide along the Jinsha River. Different from previous retrospective studies, the landslide in this work did not collapse yet. We speculate that the slope is unstable and could pose a threat to downstream areas by blocking the Jinsha River. To test this hypothesis, we used multi-temporal Sentinel-2 images to detect possible slope displacements. We first used two Sentinel-2 images to find the relatively stable period before the flood caused by the upstream Baige landslide (October and November 2018). Then, we further analysed the movement of the slope after the flood from the Baige landslide in 2019.

2 Methodology

The reported slope is ~80 km downstream the Baige landslide along the Jinsha River near Mindu town, Tibet Autonomous Region, bordering Sichuan Province (Figure 1a). The slope is located on the right bank of the Jinsha river. Similar to the Baige landslide, the geomorphology of this section of the Jinsha river is at the bottom of V-shaped valley.

The landslide is visible in the 15 m resolution pan-sharpened false colour Landsat 7 image acquired in 2001 (Figure 1b). From the image, we can see the cracked slope and signs of the mass movement, characterized by a bare surface. This part of the slope has an aspect of the southeast, with azimuth between 112.5 ° and 157.5 ° (Figure 1c). This downstream landslide around the Mindu town has a similar monsoon climate with the Baige landslide and most of the rain occurs from May to October (Yang et al. 2019).

2

This work used the COSI-Corr method, a correlation method for optical images, to detect slope displacements (Leprince et al. 2007). To derive slope movement, two image in a roll should be used to form an image pair, including the base image and the target image. The base image is an earlier image, based on which image correlation algorithm (here we use the COSI-Corr) is implemented to detect slope displacements in the target image (Leprince, et al. 2007). For detailed parameters to use the COSI-Corr method, please refer to Yang, et al. (2019b).

In this work, two steps were taken to detect slope displacements. First, we used two image pairs to detect slope movement before November 2018. For this step, we used three Sentinel-2 images on 13 November 2015, 12 November 2018 and 12 November 2019 to compose two image pairs. The first image pair is composed of a Sentinel-2 image on 13 November 2015 and a Sentinel-2 image on 12 November 2018. Sentinel-2 images of the second pair are on 12 November 2018 and on 12 November 2019. Both image pairs are composed of Sentinel-2 images of similar dates of different years to minimize the influence of solar elevation angles (Yang et al. 2020). System errors caused by image registration were estimated in the stable zone (red rectangular in Fig 1b and 1c). Both image pairs are composed by two images of very similar acquire dates of different years. Images of similar dates have similar zenith/elevation angles, which could minimize the influence of mountain shadows (Yang et al. 2020). To use image correlation methods, two types of errors should be considered: Type I system error, which is usually caused by monolithic image shifts; Type II image distortion, which is caused by orthorectification or shadow changes in different images. Type I error can be corrected by selecting a stable zone. Accurately orthorectified images acquired at a similar solar zenith/elevation angle should be used to reduce Type II error.

We further used two image groups, a base image group and a target image group, to detect slope displacements and estimate uncertainties (Table 1). For the base image group, there are 19 images, all of which are acquired in early 2018. These selected 19 base images are clear images without clouds in 2018. Although Sentinel-2 images have very short revisit time, most images are contaminated by clouds on the Mindu slope before September 2018. For the target image group, we selected five images in 2019 (13 April, 17 July, 24 August, 5 October and 12 November) to detect slope displacements. For each target image in 2019, average slope displacements and uncertainties are estimated from all 19 base images by forming 19 image pairs in the COSI-Corr method, separately. In all, there are 19×5 image pairs are calculated in the second step.

To derive spatial-temporal slope deformation patterns, we used nine images from 28 September 2018 to 7 February 2020 (Table 2) to form eight image pairs (periods) to derive slope displacements in different periods. All slope displacements were corrected by using the stable zone (the rectangular with red boundary in Figure 1b&1c). We further used the SRTM DEM derived aspect to filter out derived slope movement that does not agree with the aspect. If there are 15° deviations between the derived slope movement and the aspect, the derived slope movement is defined as not valid and will not be used for further analysis. This is reasonable for translational landslides as the mass moves downhill driven by gravity. Evidenced by optical images, the landslide in this work is a translational type and could be dealt with in this way (Highland and Bobrowsky 2013).

3 Results

3.1 Detected stable and unstable periods

In Table 3, The EW-mean and NS-mean indicate the Type I error or the shifts of images in both image pairs calculated from the stable zone. The EW-std and NS-std show part of the Type II error, which measures image distortions in the stable zone. Low EW-std and NS-std values indicates little Type II error and good performances during image orthorectifications. The derived EW-mean and NS-mean were then used to correct type I errors.

For image pair #1, the base image is acquired on 13 November 2015 and the second image is acquired on 12 November 2018. The slope remains stable in the first image pair, whereas detectable slope displacements can be found in the second image pair (Figure 2). The duration of the first image pair spans 3 years and the second image pair lasts one year. In Figure 2a, we can see that the slope displacement from 13 November 2015 to 12 November 2018 was less than 2 m, whereas there was more than 6 m slope displacement from 12 November 2018 to 12 November 2019 (Figure 2b). In image pair #2, larger displacements were observed near the Jinsha river and smaller displacements were farther away from the river. This increasing displacement magnitude may indicate the slope may start to move from its foot.

3.2 Slope displacements in 2019

As in Figure 2, we can see that the slope remains stable from November 2015 to November 2018 and is moving after November 2018. To derive time series of the Mindu slope displacements after November 2018, we used 19 base images in the stable period and 5 target images in 2019. All 19 base images are from early 2018, during which the slope was stable. Five selected target images are acquired on 13 April 2019, 17 July 2019, 24 August 2019, 5 October 2019 and 12 November 2019. For each target image in 2019, we calculated slope movement by using all base images. Therefore, there are 19 estimated slope displacements for each target image. We calculated the means and standard deviations of slope displacements for each target image representing slope movement from early 2018 and six periods in 2019 (Figure 3).

From Figure 3, we can see that the mean displacements are a magnitude larger than standard deviations, which indicate that the displacements derived between each target image and their base images agree with each other quite well. Minor slope displacements were detected until April 2019 (maximum 3~4m), whereas larger slope displacements can be observed in the later four target images (>5 m). All displacements in five target images show a similar pattern with results in image pair 2 (Figure 2b), demonstrated by larger displacements near the river and less movement further from the river. However, the third target image (24 August 2019) has more displacement of large values than other target images. As seen from Figure 3, it is quite possible that the slope moved significantly during 2019.

We further selected six points on the slope to analyse time series of the slope displacements in 2019 (Figure 4). For most target images in the first five points (p1-p5), most base images could derive >10 valid displacements (2-D columns). For all six points, accumulated displacements show similar growing trends from April 2019 to November 2019. Maximum displacements in all six points occurred on 24 August 2019. These unreasonably large values may be caused by difference of

4

solar elevation/zenith angles in target images. For example, compared to the August image there are more mountain shadows in the November images in northern hemisphere. Despite abnormal displacements in August 2019, we can still see that displacements from July to November 2019 are still larger than displacements in April 2019. Therefore, from time series of these six points, we can see that major slope displacements occurred before 13 April 2019 and from April to August 2019.

3.3 Slope displacements in eight selected periods after November 2018

To analyse spatial deformation patterns in different periods, we selected 9 Sentinel-2 images forming eight image pairs (corresponding to eight periods in ~2 months). The first two image pairs (Figure 5a-b) shows that the middle and lower parts of the slope deformed significantly and 4-6 meters of displacement occurred at multiple locations. The study area has a monsoonal climate with most precipitation occurs from May to September (Figure 6). There are seasonal differences in deformation of this landslide. In dry seasons of winter and spring, deformation occurs at the foot of the slope near the Jinsha river and deformation rate is generally less than 1 m/month (from January to May, Figure 5c&d and periods 3-4 in Figure 6). In rainy seasons of summer and autumn, deformation affects the entire slope with some parts at a rate of more than 3 meters/month (from May to September, Figure 5e&f and periods 5-6 in Figure 6).

4 Discussion

By using multi-temporal Sentinel-2 images, our work found the Mindu landslide remained relatively stable between November 2015 and November 2018 but significant slope movement occurred after November 2018. In the August 2019 target image, there are 387,200 m^2 of the Mindu slope with displacements larger than 5 m and 715,577 m^2 of the slope with displacements larger than 3 m. The Baige landslide has an area of 830,624 m^2 on the slope. River sections along both slopes are V-shape valleys. Measured in Google Earth, the width of the river at the foot of the Baige slope is more than 100 m, whereas the river width at the foot of this studied slope is ~ 50 m (Figure 7). The area of the Baige slope and the Mindu slope is similar, but the width of the river near Mindu slope is half-width of the Baige. If the Mindu landslide releases a similar volume with that of the Baige landslide, it will probably block the Jinsha river. To determine whether the landslide dam the river, landslide dam formation models should be performed in future studies (Liao et al. 2019).

There are several error sources to use optical remote sensing images to derive slope displacements. In this work, we used a stable zone to correct system errors caused by image shifts. All standard deviations of the stable zone are within 1/20 of a Sentinel-2 pixel length (0.5 m), indicating minor random errors within the stable zone. For complex mountain terrains, different solar zenith angles of two different images may also lead to false displacements (Yang et al. 2020). To reduce this type of errors, we used two Sentinel-2 images of the same date in two different years (the first image is on 12 November 2018 and the second image is on 12 November 2019). We used 19 base images in early 2018 to detect slope displacements in five target images in 2019. Our results show that standard deviations of the derived slope displacements from 19 base images are less than 1 m, indicating the robustness of using optical images to derive slope movements. The largest

5

displacements did not occur in the last target image of 2019 confirmed that different solar zenith angles may lead to errors in estimating slope displacements. Despite the influence of different solar zenith angles in different target images in 2019, the

160   overall trend of the accumulated slope displacements in our selected points is increasing, leading to our confidence to claim the movement of the Mindu slope.

      The remote sensing estimation accuracy of slope deformation needs to be improved. The currently used Sentinel 2 image has a spatial resolution of 10 meters, and the accuracy of the sub-pixel analysis results is about 2 meters. There is a certain uncertainty in the continuous monitoring of the deformation rate of different slope parts. By using high-resolution

165   (such as sub-meter high-scoring remote sensing data) image analysis, the accuracy of spatiotemporal estimation of the deformation rate of Mindu slope can be further improved.

      This work used slope aspect to filter out slope movement that is different from the aspect. This procedure could eliminate many false slope movements and reserves the true slope movement of the Mindu landslide. This method may also falsely leave out other true slope movements that have a complex structure. For example, it may fail to detect movement of

170   the head scarp of large rotational landslides, because the moving direction of the head scarp usually has a reverse direction with the slope aspect. Therefore, cautions should be taken when using slope aspect to constrain derived slope displacements.

5 Conclusions

      By using image correlation technique, we can track sub-pixel slope movement in optical remote sensing images. We adopted an aspect constraint to automatically pick out downslope movement and significantly depressed much of the

175   background noise. We applied these techniques on multi-temporal Sentinel-2 images to detect slope movement near the Mindu town along the Jinsha River. We found the Mindu landslide probably existed before 2001 and the slope remains relatively stable between November 2015 and November 2018. Significant slope displacements were observed from November 2018 to August 2019.

      We found the size of the Mindu slope that activated is similar to that of the Baige landslide, whereas the river width

180   under the Mindu slope is half of the Baige section. If the Mindu landslide continues to slide down and occur, it may block the Jinsha river leading to similar social-economic consequences as the 2018 Baige landslide. However, optical images, such as the Sentinel-2 images, can only detect slope movements up to a few metres. To derive minor slope displacements, InSAR techniques should be implemented for this remote slope. We also call for continuous monitoring of this slope and modelling of landslides caused river blocking and subsequent flooding.

185

Data availability. All Sentinel-2 images and the Landsat 8 image in this work were downloaded from the GEE. The SRTM DEM and its derivative were downloaded from the Geospatial Data Cloud website (http://www.gscloud.cn/sources).

Supplement. There is no related supplement for this paper.

References

Bontemps, N., Lacroix, P., and Doin, M.-P.: Inversion of deformation fields time-series from optical images, and application to the long term kinematics of slow-moving landslides in Peru. Remote Sens. Environ., 210, 144-158, doi: 10.1016/j.rse.2018.02.023, 2018.

Bradley, K., Mallick, R., Andikagumi, H., Hubbard, J., Meilianda, E., Switzer, A., Du, N., Brocard, G., Alfian, D., Benazir, B., Feng, G., Yun, S.-H., Majewski, J., Wei, S., and Hill, E.M.: Earthquake-triggered 2018 Palu Valley landslides enabled by wet rice cultivation. Nat. Geosci., 12, 935-939, doi: 10.1038/s41561-019-0444-1, 2019.

Du, J., Glade, T., Woldai, T., Chai, B., and Zeng, B.: Landslide susceptibility assessment based on an incomplete landslide inventory in the Jilong Valley, Tibet, Chinese Himalayas. Eng. Geol., 270, 105572, doi: 10.1016/j.enggeo.2020.105572, 2020.

Fan, X., Xu, Q., Alonso-Rodriguez, A., Subramanian, S.S., Li, W., Zheng, G., Dong, X., and Huang, R.: Successive landsliding and damming of the Jinsha River in eastern Tibet, China: prime investigation, early warning, and emergency response. Landslides, 16, 1003-1020, doi: 10.1007/s10346-019-01159-x, 2019.

Highland, L., and Bobrowsky, P.: The Landslide Handbook—a Guide to Understanding Landslides: A Landmark Publication for Landslide Education and Preparedness. Springer Berlin Heidelberg. 2013.

Intrieri, E., Raspini, F., Fumagalli, A., Lu, P., Del Conte, S., Farina, P., Allievi, J., Ferretti, A., and Casagli, N.: The Maoxian landslide as seen from space: detecting precursors of failure with Sentinel-1 data. Landslides, 15, 123-133, doi: 10.1007/s10346-017-0915-7, 2018.

Lacroix, P., Araujo, G., Hollingsworth, J., and Taipe, E.: Self-Entrainment Motion of a Slow-Moving Landslide Inferred From Landsat-8 Time Series. J. Geophys Res-Earth, 124, 1201-1216, doi: 10.1029/2018jf004920, 2019.

Lacroix, P., Bièvre, G., Pathier, E., Kniess, U., and Jongmans, D.: Use of Sentinel-2 images for the detection of precursory motions before landslide failures. Remote Sens. Environ., 215, 507-516, doi: 10.1016/j.rse.2018.03.042, 2018.

Lacroix, P., Dehecq, A., and Taipe, E.: Irrigation-triggered landslides in a Peruvian desert caused by modern intensive farming. Nat. Geosci., 13, 56-60, doi: 10.1038/s41561-019-0500-x, 2020.

Leprince, S., Barbot, S., Ayoub, F., and Avouac, J.: Automatic and Precise Orthorectification, Coregistration, and Subpixel

220 Correlation of Satellite Images, Application to Ground Deformation Measurements. IEEE T. Geosci. Remote, 45, 1529-1558, doi: 10.1109/TGRS.2006.888937, 2007.

Liao, H.-m., Yang, X.-g., Lu, G.-d., Tao, J., and Zhou, J.-w.: Experimental study on the river blockage and landslide dam formation induced by rock slides. Eng. Geol., 261, 105269, doi: https://doi.org/10.1016/j.enggeo.2019.105269.

Luo, S.-L., Jin, X.-G. & Huang, D. 2019. Long-term coupled effects of hydrological factors on kinematic responses of a

225 reactivated landslide in the Three Gorges Reservoir. Eng. Geol., 261, 105271, doi: 10.1016/j.enggeo.2019.105271, 2019.

Petley, D.: Global patterns of loss of life from landslides. Geology, 40, 927-930, doi: 10.1130/G33217.1, 2012.

Samsonov, S., Dille, A., Dewitte, O., Kervyn, F., and d'Oreye, N.: Satellite interferometry for mapping surface deformation time series in one, two and three dimensions: A new method illustrated on a slow-moving landslide. Eng. Geol., 266, 105471, doi: 10.1016/j.enggeo.2019.105471, 2020.

230 Wasowski, J., and Bovenga, F.: Investigating landslides and unstable slopes with satellite Multi Temporal Interferometry: Current issues and future perspectives. Eng. Geol., 174, 103-138, doi: 10.1016/j.enggeo.2014.03.003, 2014.

Yang, W., Wang, Y., Sun, S., Wang, Y., and Ma, C.: Using Sentinel-2 time series to detect slope movement before the Jinsha River landslide. Landslides, 16, 1313-1324, doi: 10.1007/s10346-019-01178-8, 2019.

Yang, W., Wang, Y., Wang, Y., Ma, C., and Ma, Y.: Retrospective deformation of the Baige landslide using optical remote

235 sensing images. Landslides, 17, 659-668, doi: 10.1007/s10346-019-01311-7, 2020.

Zhang, S., Li, C., Zhang, L., Peng, M., Zhan, L., and Xu, Q.: Quantification of human vulnerability to earthquake-induced landslides using Bayesian network. Eng. Geol., 265, 105436, doi: 10.1016/j.enggeo.2019.105436, 2020.
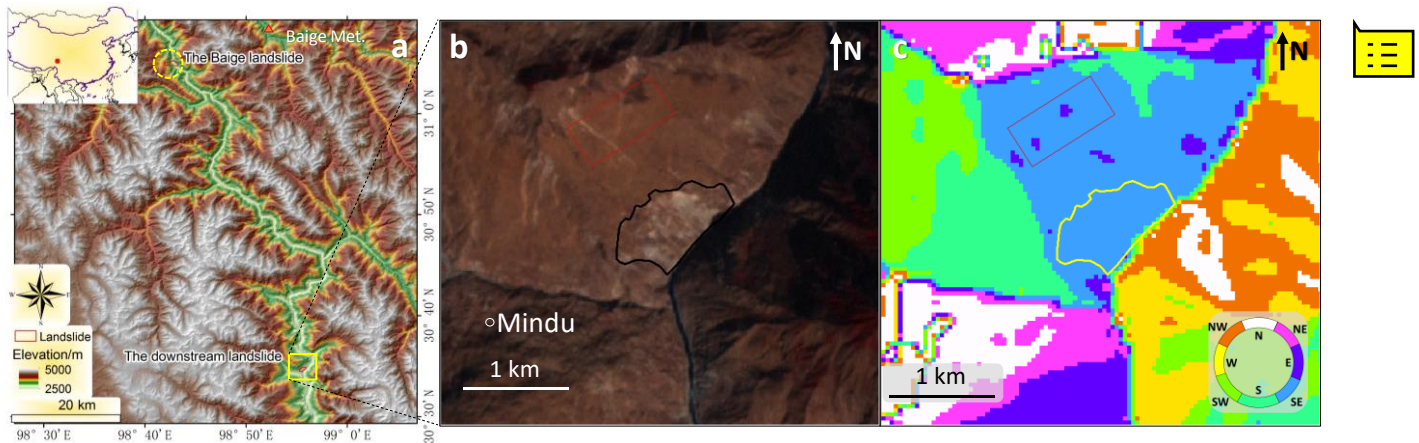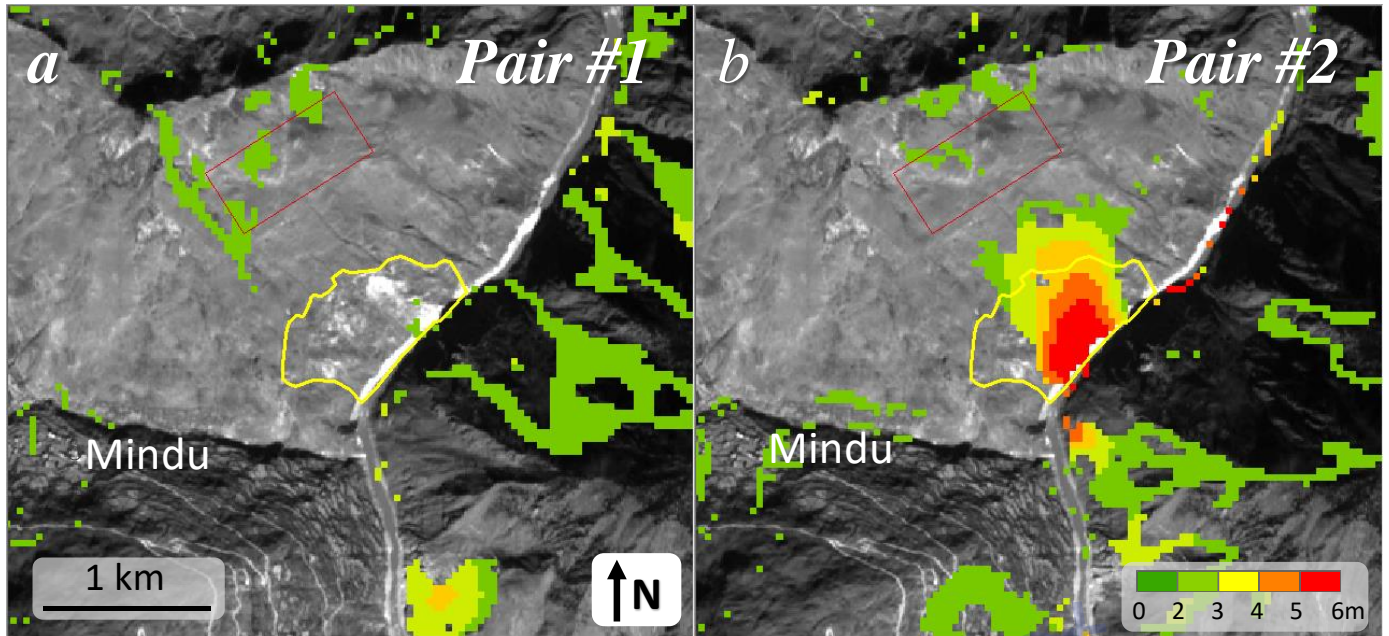
240

Figure 1: Topographic maps of the study area. (a) Geographic locations of the Baige landslide and the downstream landslide around the Mindu town, Tibet Autonomous Region. (b) A 15 m resolution pan-sharpened Landsat 7 false colour image on 18 February 2001 and aspect of the study area around the Mindu landslide (The elevation data in a is a product of the NASA's

245 **Shuttle Radar Topography Mission (SRTM) and the aspect in c is a derivative of the DEM. Both the SRTM DEM in a and its derivative c are downloaded from the Geospatial Data Cloud website (http://www.gscloud.cn/sources). The Landsat image in b is a joint product of the USGS and NASA and was downloaded via the Google Earth Engine (GEE)).**

Figure 2: Detected slope displacements in image pairs #1, #2 and #3 (Background Sentinel-2 images are acquired on 13 November 250 2015, 12 November 2018 and 23 October 2018, respectively. Both images were produced by the ESA's Sentinel-2 satellites and downloaded via the GEE).
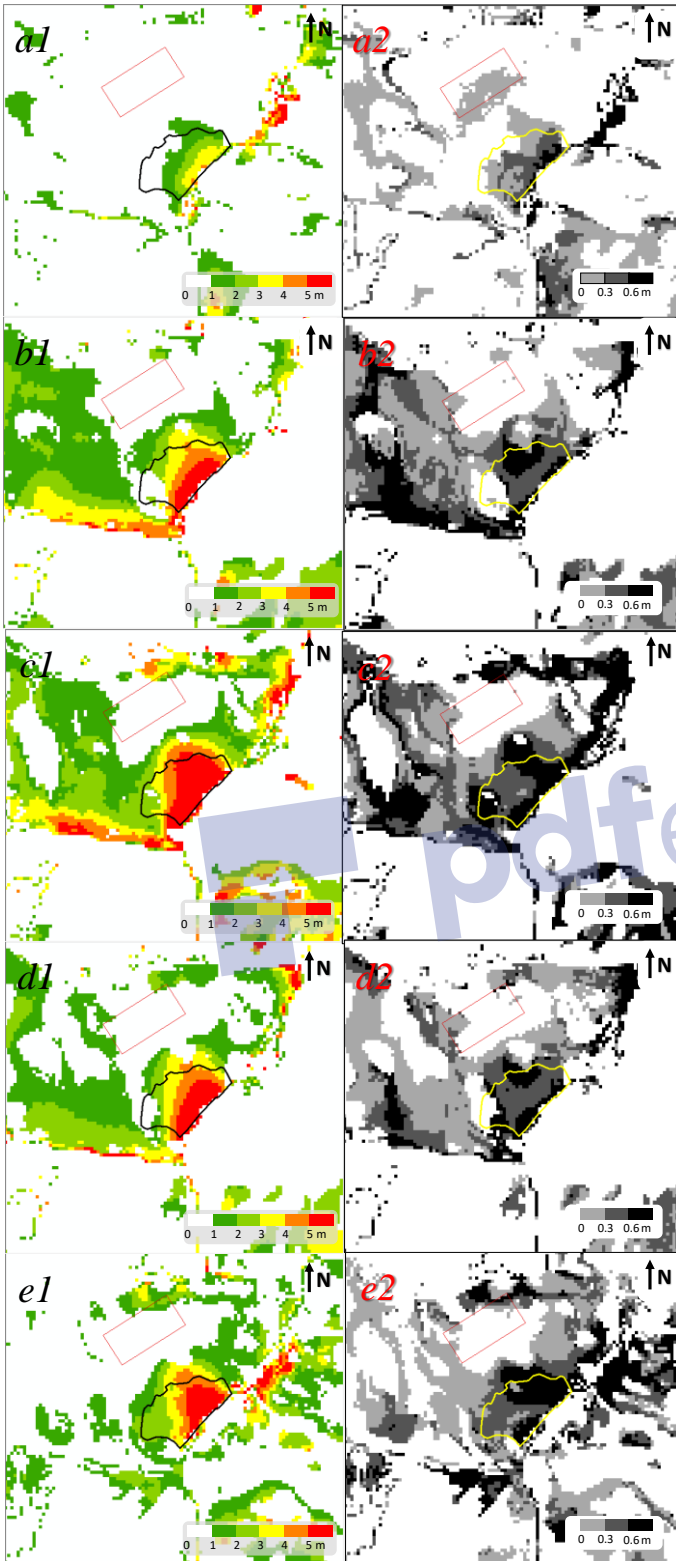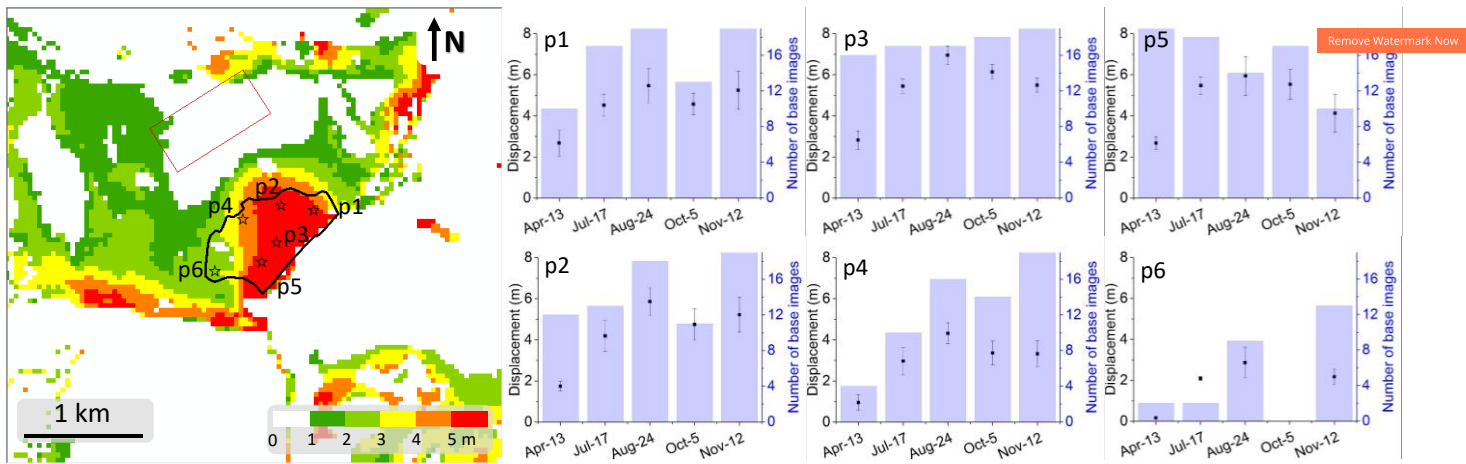
Figure 3: Means and standard deviations of derived slope displacements in nine targeted images (Tab. 2). Detected means and standard deviations of slope displacement on 18 Sep. 2018 (*a1-a2*), 23 Oct. 2018 (*b1-b2*), 28 Oct 2018 (*c1-c2*), 12 Nov. 2018 (*d1-d2*), 13 Apr. 2019 (*e1-e2*), 17 Jul. 2019 (*f1-f2*), 24 Aug. 2019 (*g1-g2*), 5 Oct. 2019 (*h1-h2*), 12 Nov. 2019 (*i1-i2*), respectively.

Figure 4: Time series of slope displacements for the six target images. Image to the left shows slope displacements shown above the Sentinel-2 image on 12 November 2019 and map colour is shown in minimum-maximum linear stretch type.
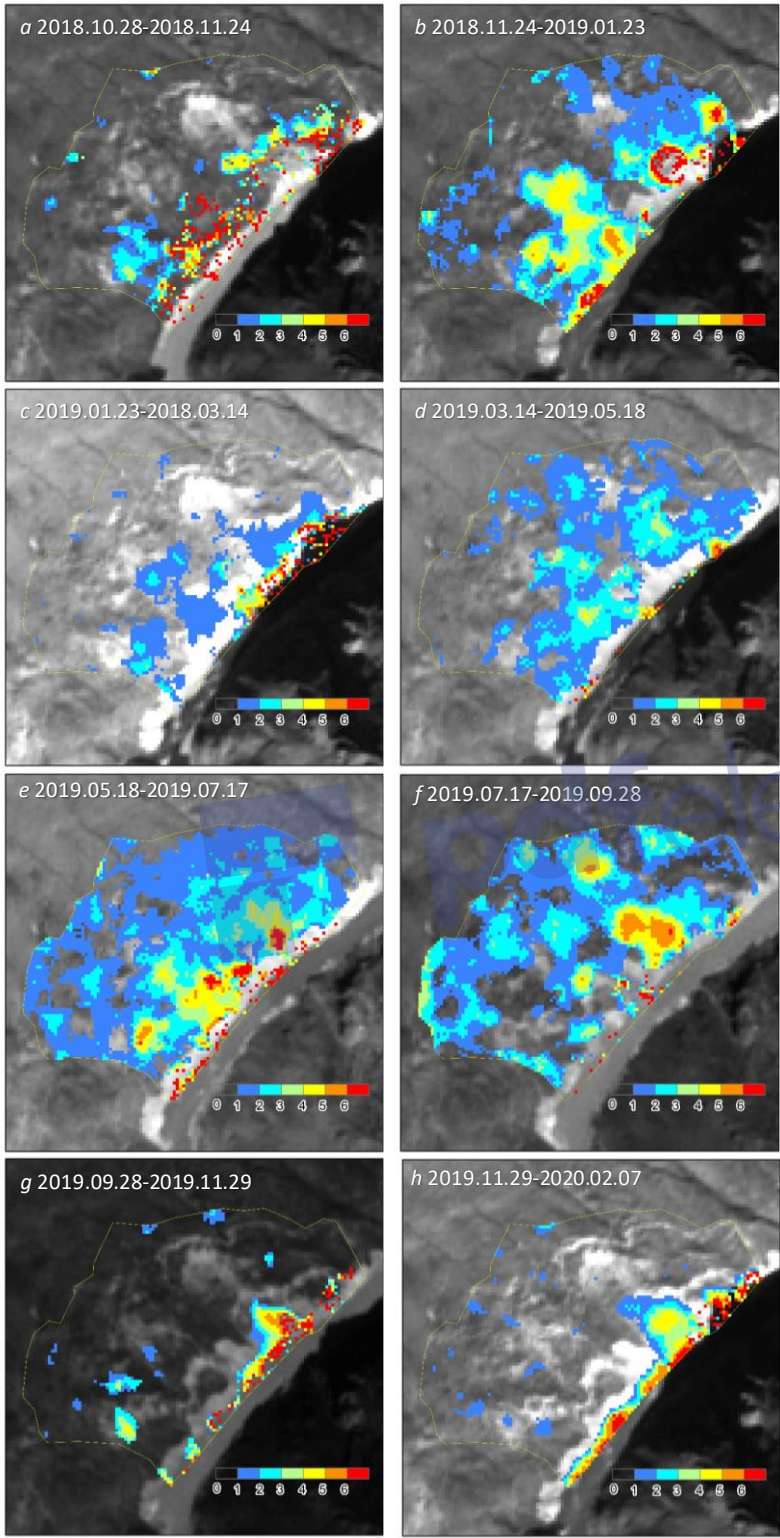
Figure 5: Slope displacements in different periods after the Baige floods (Background images are Sentinel-2 data produced by the ESA's Sentinel-2 satellites and downloaded via the GEE).
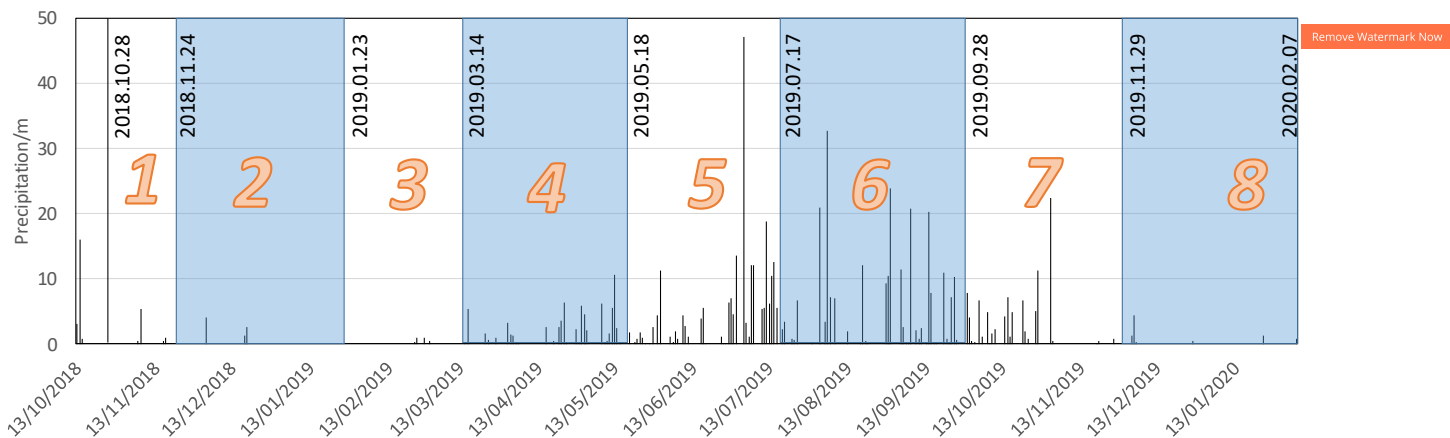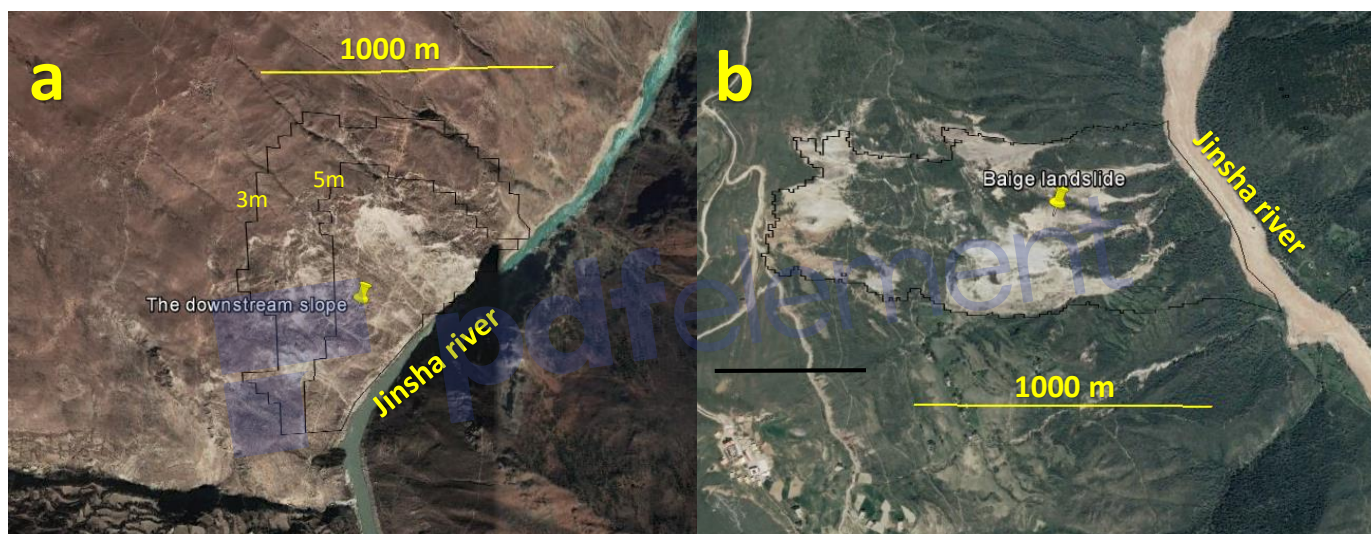
Figure 6: Daily precipitation of the Baiyu Meteorology station from October 2018 to February 2020.

Figure 7: High spatial resolution images from the ©Google Earth. The image to the left is acquired on 30 March 2015 for the Mindu slope (a) and the right image is acquired on 18 July 2017 for the Baige slope (b).

Table 1. List of 19 base images in early 2018 and 9 targeted images. Base images were used to detect slope displacements in targeted images.

19 base images in early 2018	5 target images in 2019
January: 11, 13, 16, 23, 28	
February: 5, 12, 17, 25	
March: 4, 9, 14, 19, 29	2019: 13-Apr., 17-Jul., 24-Aug., 5-
April: 3, 16, 23	Oct., 12-Nov.
May: 21	

June: 5

265

Table 2. Eight periods (image pairs) were used to derive the Mindu slope movement.

Image pairs	Base image	Target image
#1	28 Oct. 2018	24 Nov. 2018
#2	24 Nov. 2018	23 Jan. 2019
#3	23 Jan. 2019	14 Mar. 2019
#4	14 Mar. 2019	18 May 2019
#5	18 May 2019	17 Jul. 2019
#6	17 Jul. 2019	28 Sep. 2019
#7	28 Sep. 2019	29 Nov. 2019
#8	29 Nov. 2019	07 Feb. 2020

Table 3. Detected image shifts (system error) in the "stable zone". The EW-std and NS-std indicates uncertainties of the method and the EW-mean and NS-mean were used to derive the final displacements in image pairs.

Image pairs	Dates	EW-mean	EW-std	NS-mean	NS-std	snr-mean	snr-std
#1	2015.11.13 2018.11.12	-0.495077	0.181026	-7.275188	0.253885	0.989819	0.001601
#2	2018.11.12 2019.11.12	4.115833	0.056559	9.914275	0.136149	0.989803	0.001434

270

275